IEEE/CSC & ESAS EUROPEAN SUPERCONDUCTIVITY NEWS FORUM, No. 19, January 2012
LTD-14 Paper Submitted to *J. Low Temp. Physics* (*JLTP*) (should be cited accordingly)
Published in *Journal of Low Temperature Physics* Volume **167**, Numbers 3-4, pp. 269-279, (2012)

maXs: Microcalorimeter Arrays for High-Resolution X-ray Spectroscopy at GSI/FAIR

C. Pies[a] · **S. Schäfer**[a] · **S. Heuser**[a] · **S. Kempf**[a] · **A. Pabinger**[a] · **J.-P. Porst**[a,b] · **P. Ranitsch**[a] · **N. Foerster**[a] · **D. Hengstler**[a] · **A. Kampkötter**[a] · **T. Wolf**[a] · **L. Gastaldo**[a] · **A. Fleischmann**[a] · **C. Enss**[a]

Keywords MMC, metallic magnetic calorimeters, low-temperature detectors, x-ray detectors, QED effects in ions,
Abstract Highly-charged heavy ions like U^{91+} provide unique conditions for the investigation of relativistic and quantum electrodynamical effects in strong electromagnetic fields. We present two x-ray detectors developed for high-resolution spectroscopy on highly-charged heavy ions. Both detectors consist of metallic magnetic calorimeters (MMCs) forming linear eight-pixel arrays. The first detector, *maXs-20*, is developed for the detection of x-rays up to 20 keV with an energy resolution below 3 eV. The second device, *maXs-200*, is designed for x-ray energies up to 200 keV with an energy resolution of 40 eV. The results of characterization measurements of both detectors will be shown and discussed. Furthermore, we present a prototype MMC for soft x-rays with improved magnetic flux coupling. In first characterization measurements the energy resolution of this device was 2.0 eV (FWHM) for x-rays up to 6 keV.

PACS numbers: 07.20.Mc, 07.77.Ka, 07.85.Fv, 07.85.Nc, 29.40.Vj, 31.30.J-, 32.30.Rj

1 Introduction

Although quantum electrodynamics (QED) has been very well tested and confirmed in the presence of low fields, the validity of this theory at large field

a Kirchhoff-Institute for Physics, Heidelberg University,
INF 227, D-69120 Heidelberg, Germany
Tel.: +49 6221 549254
E-mail: cpies@kip.uni-heidelberg.de
b NASA Goddard Space Flight Center,
Greenbelt, MD 20771, USA

strengths is still unter question. In heavy atoms and ions, the innermost electrons are exposed to very strong electric and magnetic fields of up to 10^{16} V/cm and 10^5 T, respectively, hardly available in other systems. This makes heavy ions perfect test candidates for this regime of QED. Highly-charged heavy ions (HCI), in particular systems with three or less electrons, are of special interest for spectroscopic experiments, since theory can be provided much easier as for neutral atoms or many-electron ions.

Currently, such spectroscopic experiments on HCI are performed at GSI Darmstadt [1]. There, for example, bare uranium nuclei (U^{92+}) are injected into a storage ring with relativistic velocities. After traversing a gas jet target, the ion is down-converted to hydrogen-like U^{91+} (i.e. a uranium ion with only one electron) while the captured electron performs a cascading transition towards the ground state, emitting the energy differences in the form of (Doppler-shifted) photons. In such heavy ions, typical energy differences between the lowest levels are in the range of several to several tens of keV, but due to the Doppler effect, the detected photons can also have energies above 100 keV, depending on the angle of observation with respect to the beam.

The future *Facility for Antiproton and Ion Research* (FAIR) at GSI will offer unique facilities for QED tests on HCI. Amongst others, it will be possible to decelerate the ions to significantly lower velocities than presently available, even down to rest. Furthermore, the new facility will provide a larger ion flux, allowing for higher statistics in the measurements.

The x-ray photons emitted during the transition cascade of the captured electron, are presently detected with crystal spectrometers, germanium detectors and silicon thermistors. Detectors based on metallic magnetic calorimeters (MMCs) [2] are planned to extend the assortment of measuring devices.

We present two prototype MMC detectors developed for high-resolution x-ray spectroscopy on HCI. The first detector design, *maXs-20*, is optimized for the detection of x-rays up to 20 keV with a designed energy resolution below 3 eV. The second detector, *maXs-200*, is designed for x-ray energies up to 200 keV with an energy resolution of 40 eV.

2 *maXs-20*

2.1 Detector Design

Figure 1 shows a scanning electron microscope picture of the present version of the *maXs-20* detector chip. The detector consists of a linear array of eight pixels (i.e. four gradiometric MMCs with meander-shaped pickup coils [2]) with an absorber size of 250×250 μm^2 and a gap of 5 μm in between pixels. For future experiments at GSI/FAIR, this linear array might get rearranged to form a compact two-dimensional array to be positioned in the focus of an x-ray lens.

Gold is used as an absorber material due to its high stopping power for photons. A thickness of 5 μm provides a stopping power close to 100 % for photons of energies up to 6 keV and 45 % at 20 keV. In figure 2 the full energy absorption efficiency of the absorber in *maXs-20* is shown as calculated with Monte Carlo simulations using the software PENELOPE [3].

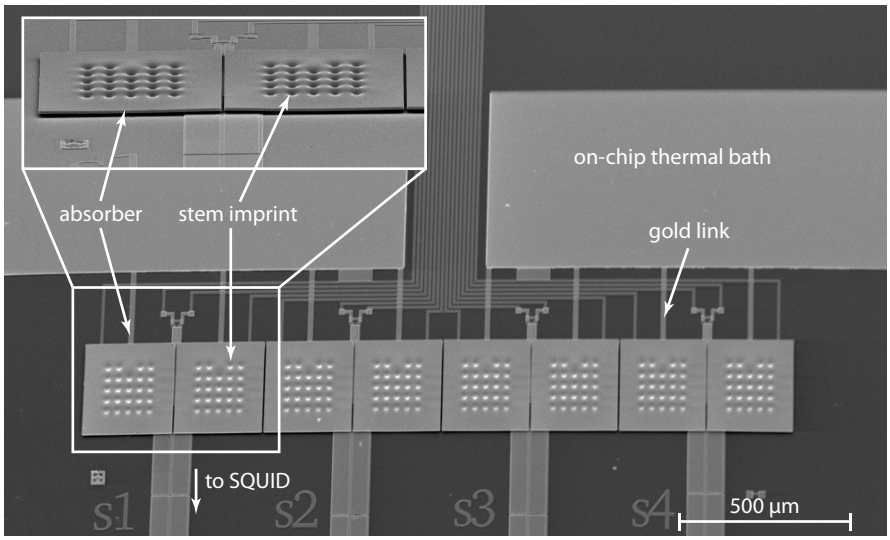

Fig. 1 SEM picture of *maXs-20*. Description in the text.

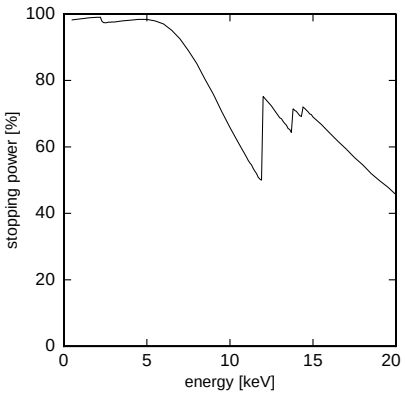

Fig. 2 Full energy stopping power of the 5 µm thick gold absorber of *maXs-20* as simulated with PENELOPE.

Each absorber is connected to a $160 \times 160 \times 1.3\ \mu m^3$ paramagnetic temperature sensor, Au:^{168}Er$_{300\ ppm}$, through twenty-four 5 µm thick gold stems, visible in the picture as imprints in the absorbers. The presence of these stems reduces the contact area between sensor and absorber to about 7 % of the sensor area. This geometry helps in decreasing the energy loss due to escaping high-energetic (athermal) phonons, which otherwise can lead to low energy tails of the spectral lines [4].

In order to tune the decay time of the thermal pulses, each paramagnetic sensor is linked by a sputter deposited gold stripe to an on-chip thermal bath. The thermal conductance of the link is designed to yield relaxation times of the MMC of 3 ms at an operating temperature of 30 mK.

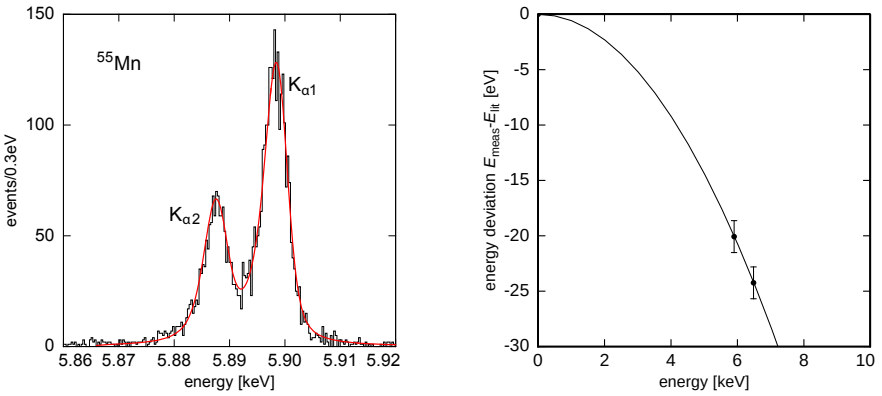

Fig. 3 (Color online) Left: ^{55}Mn K$_\alpha$ line acquired with *maXs-20* (histogram), natural line shape convoluted with a gaussian of $\Delta E_{\mathrm{FWHM}} = 3.4$ eV (solid red line). **Right:** Deviation from linear detector response for *maXs-20*. The error bars correspond to the variance of the gaussian convoluted with the natural line shape.

The detectors are completely microfabricated using sputter deposition and, for the gold absorbers, galvanization processes. A detailed description of the fabrication process of an MMC similar to *maXs-20* can be found in [4].

2.2 Performance

The characterization of the *maXs-20* detector was performed in a pulse tube cooled adiabatic demagnetization refrigerator (VeriCold Technologies, now Oxford Instruments, Abingdon, UK) with x-ray windows in all thermal shields and the vacuum can using an external ^{55}Fe calibration source. The detector was read out with a two-stage SQUID configuration (C4X116; PTB, Berlin, Germany; input coil inductance 1.6 nH) [5] and the signal was amplified and linearized by an XXF-1 electronics by Magnicon Gbr (Hamburg, Germany) [6].

Figure 3 left shows the K$_\alpha$ line of ^{55}Mn recorded with one pixel of *maXs-20* at a temperature of 30 mK. The solid red line represents the natural line shape convoluted with a gaussian with a full width at half maximum of $\Delta E_{\mathrm{FWHM}} = 3.4$ eV representing the instrumental line width. Simultaneously with the ^{55}Mn spectrum, random untriggered noise signals were acquired. Applying the data reduction algorithm, as used to assign a photon energy to the triggered detector events, to these untriggered noise records results in a line in the energy spectrum which is centered around zero energy, has gaussian shape and a width of $\Delta E_{\mathrm{FWHM}} = 3.0$ eV.

One can see that the fitted curve in figure 3 left does not exactly match the measured data at the low-energy slope of the Mn K$_\alpha$ line. This might be explained by the loss of energy to the substrate of the detector due to athermal phonons as described before. Although the contact area between sensor and absorber was already reduced to 7 % by the use of stems, a further reduction seems necessary within the next generation of *maXs-20* to overcome this residual low energy tail of the x-ray energy lines.

From optimization calculations which lead to the detector layout discussed here, the energy resolution of this device is expected to be 2.1 eV. The deviation between calculated and measured energy resolution can be explained by two facts. Firstly, the inductance of the meander-shaped pickup coils in the detector and the stray inductances between detector and SQUID are about 60 % larger than calculated from finite element simulations. Secondly, an additional heat capacity of 0.3 pJ/K (about 10 % of the total heat capacity) is found for this device. The origin of this heat capacity is not clear, but there are strong indications that it is located in the sputter deposited Au:Er sensors and in the sputtered gold seed layer needed for the electrodeposition of the absorbers [4]. Including these two effects in the numerical calculations, the predicted energy resolution of *maXs-20* is degraded to 3.0 eV, in good agreement with the measured value extracted from untriggered noise records.

As expected for MMCs, the energy resolution hardly depends on energy as long as the position dependence of the detector response, the loss of athermal phonons, and the variation of the overall signal gain are kept small, and as long as the detector response depends linearly on the photon energy.

In the case of *maXs-20*, the absorption of a 6 keV photon creates a temperature rise of about 0.3 mK if the detector is operated at 30 mK. On this level, the detector sensitivity can not be considered temperature independent. This causes the detector signal amplitude to deviate by about -0.3 % from a linear dependence on energy. The right diagram in figure 3 shows the measured deviation between detected and real photon energy for *maXs-20*, in good agreement with the expected value from the temperature dependence of the heat capacity and the sensor magnetization of the device.

3 *maXs-200*

3.1 Detector Design

An optical and SEM picture of the *maXs-200* detector chip is shown in figure 4. The detector covers an active area of 8 mm^2, divided into a linear array of eight pixels (i.e. four gradiometric MMCs) with each pixel having a width of 500 μm. With this width, the detector performance will not be limited by the broadening of lines due to Doppler effect for relativistic ion beams in the case that the diameter of the internal gas jet target in the Experimental Storage Ring ESR at GSI is reduced to a similar size in the future. The pixel's length was chosen to be 2 mm to obtain a detection area of 1 mm^2 per pixel. The separation between pixels measures 50 μm, leading to a filling factor of 92 %.

In order to provide sufficient stopping power for x-rays up to 200 keV, the absorbers of the *maXs-200* detector are designed to be made of 200 μm thick gold. However, a mistake in the timing during the galvanization process lead to a reduced absorber thickness of 140 μm for the detector discussed here. As shown in the left of figure 5, this reduced thickness leads to a full energy stopping power of close to unity for x-ray energies up to 40 keV, 45 % at 100 keV and 12 % at 200 keV.

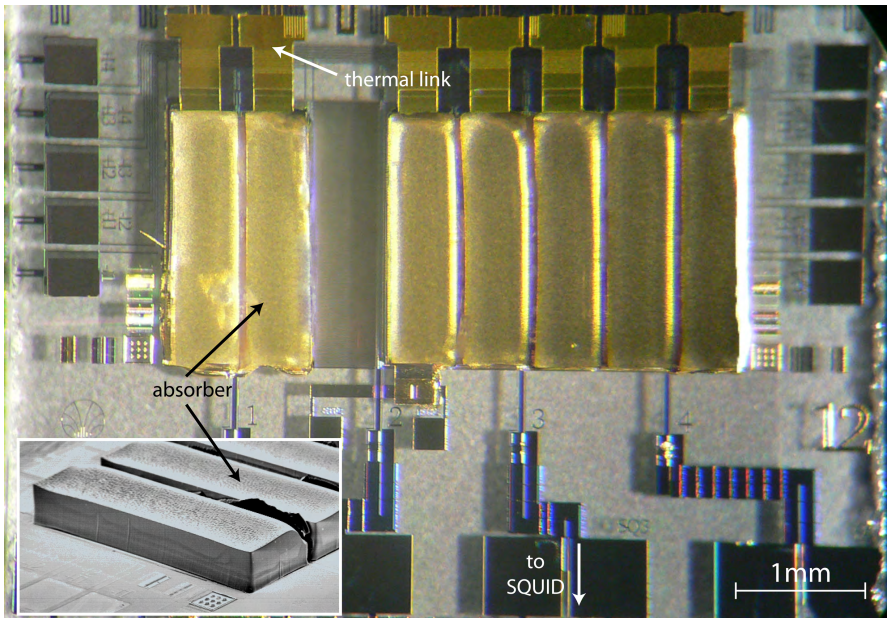

Fig. 4 (Color online) Optical and SEM picture of *maXs-200*. Description in the text.

The absorber of *maXs-200* has full contact to the 2.4 µm thick Au:^{168}Er$_{885\ \mathrm{ppm}}$ sensor. However, we developed a method to have gold stems between sensor and absorber in the next generation of produced *maXs-200* chips.

Each sensor is individually heat sunk by a gold stripe and gold wire bonds to the thermal bath. The design parameters of the thermal link lead to a signal decay time constant of 28 ms at a temperature of 20 mK.

A detailed description of the microfabrication of a prototype *maXs-200* detector is given in [7].

3.2 Performance

The detector was characterized in a dilution refrigerator in two measuring runs, once with an ^{55}Fe and once with an ^{241}Am calibration source, respectively. A two-stage SQUID (C4XS116W; PTB; input inductance 23.2 nH) and an XXF-1 electronics (Magnicon Gbr) were used to read out the detector signals.

The right diagram of figure 5 shows the ^{55}Mn K_α and K_β lines acquired at a temperature of 20 mK. The superimposed red line corresponds to the natural line shape convoluted with a gaussian with a width of $\Delta E_{\mathrm{FWHM}} = 40$ eV representing the instrumental line shape to fit the measured data. The same value is received at zero photon energy for untriggered noise traces. This corresponds to the detector performance as expected from optimization calculations at an operating temperature of 20 mK.

In figure 6 the ^{237}Np L lines, i.e. x-ray fluorescence photons emitted after the α decay of ^{241}Am, measured in a second experiment are shown. A sum of lorentzian

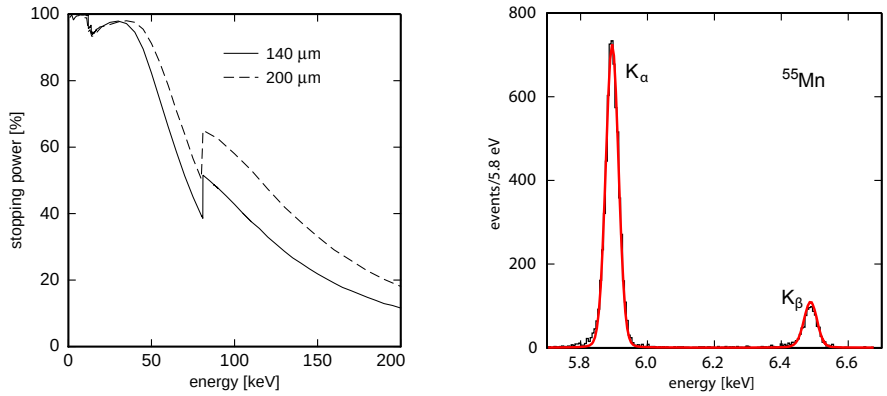

Fig. 5 (Color online) Left: Full energy stopping power of the gold absorber of *maXs-200* as simulated with PENELOPE. **Right:** ^{55}Mn K_α and K_β lines acquired with *maXs-200* (histogram), natural line shape convoluted with a gaussian of $\Delta E_{\mathrm{FWHM}} = 40$ eV (solid red line).

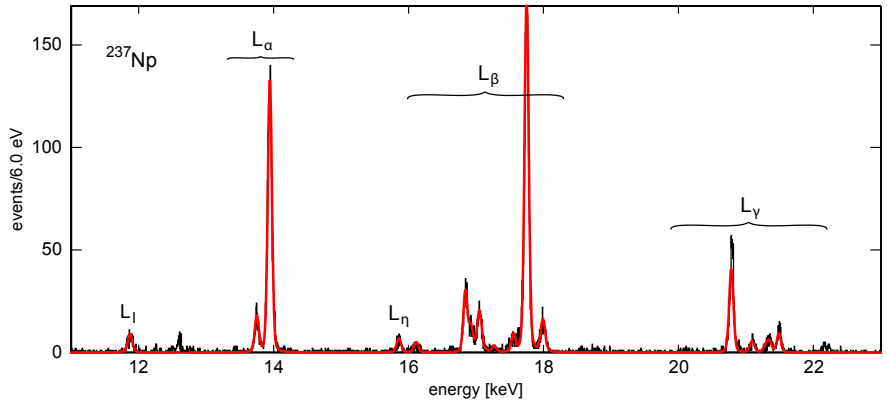

Fig. 6 (Color online) ^{237}Np L fluorescence lines from the ^{241}Am source acquired with *maXs-200* (histogram), natural line shape convoluted with a gaussian of $\Delta E_{\mathrm{FWHM}} = 60$ eV (solid red line).

functions for the different lines in the spectrum was convoluted with a gaussian function to fit the data (solid red line). The natural widths of the lines were taken from [8], whereas the relative amplitudes and the position were free parameters in the fit. We find that the data is described best with an instrumental energy resolution of $\Delta E_{\mathrm{FWHM}} = 60$ eV. The same value is observed when fitting a gaussian function to the main gamma line of ^{241}Am, as shown in figure 7 left. Furthermore, the measured baseline distribution of this particular experiment shows the same width of 60 eV.

The deviation in performance observed in the two experiments, where the same *maXs-200* detector was used, can be explained by differences in the experimental conditions. When characterized with x- and γ-ray photons of the ^{241}Am source, the SQUID noise was larger than when measuring with the ^{55}Fe source. In

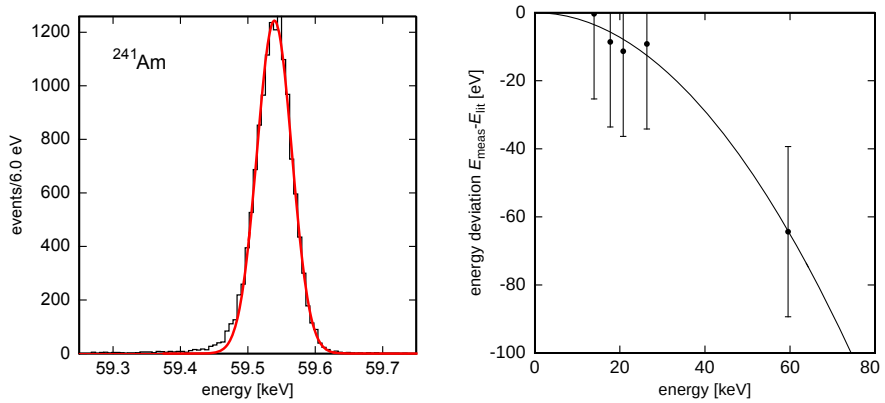

Fig. 7 (Color online) Left: Main gamma line of ^{241}Am acquired with *maXs-200* (histogram) and gaussian fit with $\Delta E_{\mathrm{FWHM}} = 60$ eV (solid red line). **Right:** Deviation from linear detector response for *maXs-20* and *maXs-200*. The error bars correspond to the standard deviation of the fitted gaussian functions.

addition, the average power produced by the decay of ^{241}Am (370 kBq, 5.6 MeV per decay, mostly given to α particles absorbed by the source housing) of about 300 nW lead to a slightly higher working temperature of the cryostat.

As in *maXs-20*, a small but clearly visible excess of events can be seen at the low-energy side of the lines which is probably due to the loss of energy to the substrate through high-energetic athermal phonons for the small fraction of events where the photon is absorbed close to the interface between absorber and sensor. As mentioned before, this effect will be reduced in the next generation of detectors by connecting the absorber to the sensor only through stems.

Due to its comparibly large heat capacity of about 630 pJ/K at 20 mK, the temperature rises after the absorption of a photon in the *maXs-200* detector are about 250 times smaller than in *maXs-20*. Therefore, the nonlinearity of the detector response is significantly smaller. From the thermodynamical properties of the detector, the signal of a 60 keV photon is expected to be about 0.1 % lower than predicted from a perfectly linear detector response. The right diagram in figure 7 shows the measured deviation between detected and real x-ray energy for the major lines emitted by the ^{241}Am source, agreeing well with the expectation. The error bars correspond to the variance of the gaussians which are convoluted with the natural line shapes.

4 Alternative MMC Geometry

In *maXs-20* and *maXs-200* as well as in all previously completely microfabricated MMCs of our group [4], the paramagnetic temperature sensor is positioned on top of a meander-shaped pickup coil [9]. The pickup coil itself carries a persistent current and is thus used to create the magnetic field which polarizes the spins in the sensor. The resulting magnetic field is strongly inhomogeneous and about half of the magnetic field energy is contained within the sensor volume.

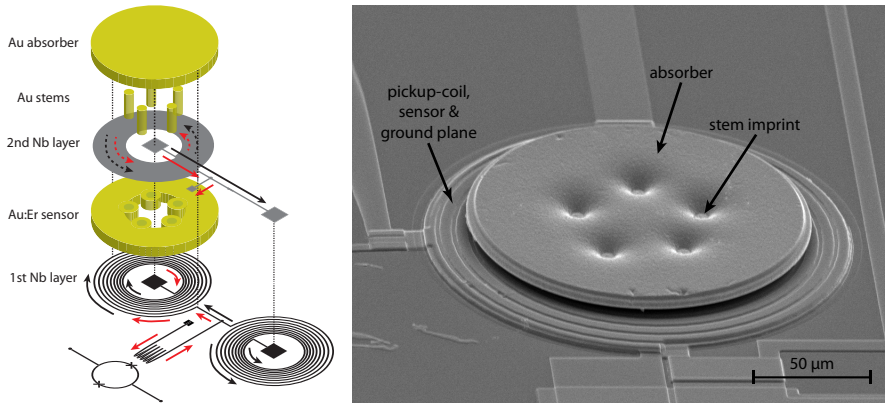

Fig. 8 (Color online) Exploded sketch (left) and SEM picture of an MMC with the sensor sandwiched between a spiral and a ground plane.

The magnetic coupling between sensor and pickup coil, and thereby the detector sensitivity, would increase if a larger fraction of the magnetic field energy were contained within the sensor. A magnetic filling factor close to unity can be realized by sandwiching the sensor between two superconducting planes which together form the pickup coil [4], or alternatively by placing the sensor on top of a spiral-shaped pickup coil and covering it with a superconducting ground plane [10].

Based on these considerations, we recently developed a prototype device, which shares most details with the "pancake coil + superconductor" device suggested and numerically treated by Boyd and Cantor in [10]. We revisited the numerical optimization of such a device including all known material properties and boundary conditions, analogous to the discussion in [4]. In the resulting device the pickup coil is formed by a spiral below and a ground plane above a ring shaped Au:$^{168}Er_{280\ ppm}$ sensor, as shown in the exploded sketch and in the SEM picture in figure 8. The sensor has an outer diameter of 170 µm and a thickness of 0.6 µm. A 5 µm thick gold absorber with a diameter of 135 µm is positioned on five stems connected to the ring-shaped sensor along its inner circumference. A second coil connected in parallel serves as a load inductor needed to prevent the field-generating persistent current from running through the input coil of the SQUID. The black and red arrows in the sketch illustrate the paths of the persistent current and of the signal current after the absorption of a photon, respectively.

The detector was installed in an adiabatic demagnetization refrigerator, irradiated with an ^{55}Fe source and read-out with a two-stage SQUID-setup (C4X1 and C4X16; PTB; input inductance 1.8 nH) and an XXF-1 electronics (Magnicon Gbr). Figure 9 shows the acquired ^{55}Mn K_α line on the left and the distribution of energies assigned to simultaneously recorded untriggered noise traces on the right. The red curve superimposed onto the histogram of the K_α line corresponds to a convolution of the natural line shape with a gaussian with $\Delta E_{FWHM} = 1.96$ eV, representing the instrumental line width. The untriggered noise events show a gaussian distribution of $\Delta E_{FWHM} = 1.8$ eV.

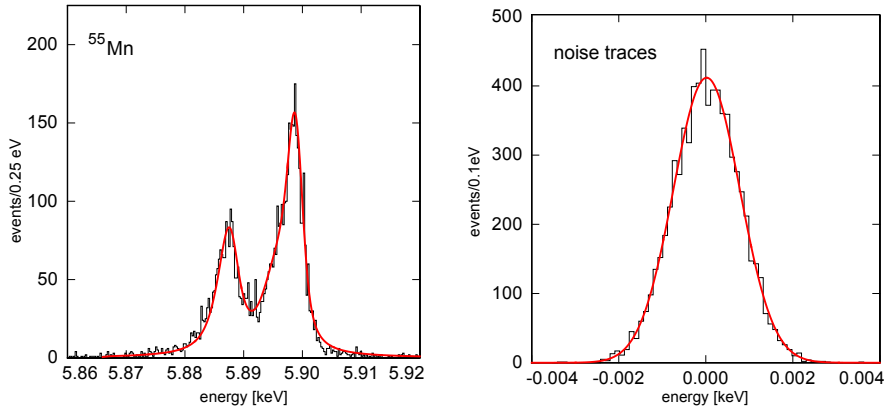

Fig. 9 (Color online) Left: ^{55}Mn K$_\alpha$ line acquired with the prototype sandwich MMC (histogram), natural line shape convoluted with a gaussian of $\Delta E_{\mathrm{FWHM}} = 1.96$ eV (solid red line). **Right:** Distribution of untriggered noise traces recorded with the prototype sandwich MMC (histogram), gaussian fit with $\Delta E_{\mathrm{FWHM}} = 1.8$ eV (solid red line).

From numerical calculations, this detector should be able to provide an energy resolution of $\Delta E_{\mathrm{FWHM}} = 0.9$ eV at 30 mK. The deviation from the measured resolution can be explained by a large parasitic magnetic flux noise most likely caused by the SQUID and, as in *maXs-20*, by a slightly increased heat capacity and somewhat increased stray inductance. Further characterization measurements using a SQUID with lower $1/f$ noise should provide energy resolutions closer to the expected value in the near future. However, it could be shown already that an MMC with a sandwich geometry can offer a huge potential for improvements of presently used devices.

5 Conclusion

The characterization measurements show that *maXs-20* and *maXs-200* perform close to their design values. This makes these two MMC based detectors promising devices to extend the possibilities of spectroscopy on highly-charged heavy ions at the present GSI and the future FAIR facilities.

Further characterization measurements of the *maXs* detector prototypes will be performed in the near future, up to the operation of a full array. Furthermore, the existing designs will be improved, amongst others introducing stems between the sensors and absorbers of *maXs-200* and increasing the size of the arrays. Since the prototype sandwich MMC provided promising first results, we plan to realize a *maXs-20* design with a similar sensor and pickup coil geometry to access energy resolutions below 2 eV.

Acknowledgements The authors wish to thank T. Stöhlker, J. Crespo, I. Uschmann and E. Förster for their support and fruitful discussions. This work was supported by the BMBF grant 06 HD 9118I, the GSI R&D grant HDEnss, and the European Community Research Infrastructures under the FP7 Capacities Specific Programme, MICROKELVIN project number 228464.

References

1. Th. Stöhlker, A. Gumberidze, A. Kumar, R. Reuschl, M. Trassinelli, *Advances in Quantum Chemistry*, **53**, ed. S. Salomonson, E. Lindroth, pp. 57-65 (2008).
2. A. Fleischmann, C. Enss, G.M. Seidel, *Cryogenic Particle Detection*, ed. C. Enss, *Topics in Applied Physics*, **99**, pp. 151–216 (2005).
3. F. Salvat, J.M. Fernández-Varea, J. Sempau, *PENELOPE-2008: A Code System for Monte Carlo Simulation of Electron and Photon Transport*, OECD Publications, ISBN 978-92-64-99066-1 (2008).
4. A. Fleischmann, L. Gastaldo, S. Kempf, A. Kirsch, A. Pabinger, C. Pies, J.-P. Porst, P. Ranitzsch, S. Schäfer, F. v. Seggern, T. Wolf, C. Enss, G.M. Seidel, *AIP Conference Proceedings*, **1185**, pp. 571–578 (2009).
5. D. Drung, C. Assmann, J. Beyer, A. Kirste, M. Peters, F. Ruede, T. Schurig, *IEEE Transactions on Applied Superconductivity*, **17**, pp. 699–704 (2007).
6. D. Drung, C. Assmann, J. Beyer, A. Kirste, M. Peters, F. Ruede, T. Schurig, C. Hinnrichs, H.-J. Barthelmess, *IEEE/CSC & ESAS European Superconductivity News Forum*, **1**, ST2 (2007).
7. C. Pies, A. Pabinger, S. Kempf, A. Fleischmann, L. Gastaldo, C. Enss, *AIP Conference Proceedings*, **1185**, pp. 603–606 (2009).
8. E. Schönfeld, U. Schötzing, *Applied Radiation and Isotopes*, **54**, pp. 785–791 (2001).
9. B.L. Zink, K.D. Irwin, G.C. Hilton, D.P. Pappas, J.N. Ullom, M.E. Huber, *Nuclear Instruments and Methods in Physics Research Section A*, **520**, pp. 52–55 (2004).
10. S.T.P. Boyd, R.H. Cantor, *AIP Conference Proceedings*, **1185**, pp. 595–598 (2009).